Tunneling current density within Tersoff and Hamann's theory of the scanning tunneling microscope

C. R. Leavens and G. C. Aers
Division of Physics, National Research Council of Canada, Ottawa, Canada K1A 0R6
(Received 13 January 1988)

Lang has extended the transfer Hamiltonian theory to obtain an expression for the tunneling current *density* and used it to investigate the current distribution in the vacuum region between pairs of jellium-adatom electrodes. In this paper, his general expression is specialized by incorporating Tersoff and Hamann's model for the tip electrode. The resulting simple expression for the tunneling current density is applied to Tersoff's six-plane-wave model of a monolayer of graphite. The normal component of the current density for this system takes on both positive and negative values in a complex flow pattern and its lateral falloff away from the (projected) tip position is much slower than expected from the extraordinary lateral resolution (~ 1 Å) evident in the scanning-tunneling-microscope images of graphite.

I. INTRODUCTION

The theoretical studies of the scanning tunneling microscope (STM) carried out by Tersoff and Hamann[1] and by Lang[2-6] are both based on Bardeen's tunneling Hamiltonian approximation.[7] Their basic approaches differ mainly in the models used for the electrodes. Tersoff and Hamann modeled the sharp end of the tip electrode by a spherical potential well but placed no restrictions on the sample electrode.[8] Lang, on the other hand, modeled each of the electrodes by a jellium half-space, with an adsorbed atom on the tip electrode or on both electrodes. Tersoff and Hamann's simple choice of tip wave function led to the important result that, at zero temperature and small bias, the tunneling current in the STM is proportional to the local electronic density of states at the Fermi energy. Lang's numerical calculations[3] with jellium-adatom electrodes gave strong support to this result.

Lang[2-4] extended Bardeen's theory to obtain an expression for the current density within the tunneling Hamiltonian approximation and calculated the current distribution in the vacuum gap between his model STM tip and a jellium electrode both with[3] and without[2,4] an adsorbed atom. A disadvantage[6] of his adatom-on-jellium model of a STM tip is that the contributions to the total current due to electrons tunneling between the jellium substrates and between the sample adatom and the jellium substrate of the tip, when the tip and sample adatoms are far apart laterally, are greatly enhanced over what they would be for the usual model of a sharp STM tip. Although Lang eliminated these unwanted contributions to a large extent by appropriate normalization, it would be useful to investigate the distribution of tunneling current using Tersoff and Hamann's model for the tip electrode. (This model has its own disadvantages[1] but these are largely compensated by its simplicity.) As a basis for such a complementary study, an expression for the tunneling current density within the Tersoff-Hamann theory is derived from Lang's more general expression in Sec. II. This is applied to a jellium sample in Sec. III and to Tersoff's six-plane-wave model[9] for a monolayer of graphite in Sec. IV. Concluding remarks are made in Sec. V.

II. TUNNELING CURRENT DENSITY IN TERSOFF AND HAMANN'S THEORY

Lang's result[2-4] for the zero-temperature, small-bias, tunneling current density in the vacuum region not too close to either the sample (s) or tip (t) electrode is given by

$$\mathbf{j}(\mathbf{r})=\frac{\pi e^2 V}{2\hbar}\int' d\nu \int' d\mu\, \delta(E_\nu - E_F)\delta(E_\mu - E_F) J_{\nu\mu}\mathbf{j}^*_{\nu\mu}(\mathbf{r}) , \tag{1}$$

$$\mathbf{j}_{\nu\mu}(\mathbf{r})=-i\frac{\hbar^2}{2m}[\psi^{(s)}_\nu(\mathbf{r})^*\nabla\psi^{(t)}_\mu(\mathbf{r})-\psi^{(t)}_\mu(\mathbf{r})\nabla\psi^{(s)}_\nu(\mathbf{r})^*] , \tag{2}$$

$$J_{\nu\mu}=\int_{-\infty}^{+\infty} dx' \int_{-\infty}^{+\infty} dy' \mathbf{j}_{\nu\mu}(\mathbf{r}')\cdot\hat{\mathbf{z}} \quad (\mathbf{r}'\equiv\mathbf{R}'+z'\hat{\mathbf{z}}) , \tag{3}$$

$$\int' d\mu\, F[\psi^{(t)}_\mu(\mathbf{r})]\equiv\int d\mu\{F[\psi^{(t)}_\mu(\mathbf{r})]+F[\psi^{(t)}_\mu(\mathbf{r})^*]\} , \tag{4}$$

where e and m are the charge and mass of the electron and V is the applied bias voltage. For definiteness the sign of V will always be chosen so that the current flows from tip to sample. The surface selected for the evaluation of $J_{\nu\mu}$ is the plane $z'=$const lying completely in the vacuum region between the electrodes. The basic ingredients in the calculation of $\mathbf{j}$ are the wave functions $\psi^{(s)}_\nu(\mathbf{r})$ and $\psi^{(t)}_\mu(\mathbf{r})$ of the isolated sample and tip electrodes, calculated in the absence of an electric field and with the actual work functions $\Phi^{(s)}$ and $\Phi^{(t)}$ replaced by the average value $\overline{\Phi}\equiv(\Phi^{(s)}+\Phi^{(t)})/2$ to ensure that $\mathbf{j}(\mathbf{r})$ is indeed independent of z'.

In Tersoff and Hamann's theory[1] of the scanning tunneling microscope the wave function of the tip electrode is modeled after the $l=0$ component of the wave function of a spherical potential well with center $\mathbf{r}_t$, radius R_0, and depth $V_0=E_F+\overline{\Phi}$, i.e.,

$$\psi^{(t)}_\mu(\mathbf{r})=c(R_0)\frac{e^{-\kappa|\mathbf{r}_t-\mathbf{r}|}}{\kappa|\mathbf{r}_t-\mathbf{r}|} \quad (|\mathbf{r}-\mathbf{r}_t|>R_0) , \tag{5}$$

where $\kappa\equiv[2m(V_0-E)]^{1/2}/\hbar$ and $c(R_0)\equiv c_t\Omega_t^{-1/2}\kappa R_0\exp(\kappa R_0)$ with Ω_t the volume of the tip and c_t of order unity. For the wave function of the sample electrode they used a completely general expression[8]

for a two-dimensionally periodic system in the region of negligible potential far enough from the surface, i.e.,

$$\psi_\nu^{(s)}(\mathbf{r})=\Omega_s^{-1/2}\sum_{\mathbf{G}} a_\nu(\mathbf{G})e^{-\alpha_{\mathbf{K}}(\mathbf{G})z}e^{i(\mathbf{G}+\mathbf{K})\cdot\mathbf{R}} \quad (z>0)\ , \tag{6}$$

where

$$\alpha_{\mathbf{K}}(\mathbf{G})\equiv[\kappa^2+(\mathbf{G}+\mathbf{K})^2]^{1/2}\ . \tag{7}$$

Here $\mathbf{G}$ and $\mathbf{K}$ are a two-dimensional reciprocal-lattice vector and Bloch wave vector, respectively. When (5) and (6) are substituted into (2) and (3) the following surface integrals, which have been evaluated by Tersoff and Hamann,[1] appear:

$$I_\pm(\mathbf{G}+\mathbf{K};z')\equiv\int_{-\infty}^{+\infty}dx'\int_{-\infty}^{+\infty}dy'\frac{e^{-\kappa_F|\mathbf{r}_t-\mathbf{r}'|}}{|\mathbf{r}_t-\mathbf{r}'|}e^{\pm i(\mathbf{G}+\mathbf{K})\cdot\mathbf{R}'}$$
$$=2\pi\frac{e^{-[\kappa_F^2+(\mathbf{G}+\mathbf{K})^2]^{1/2}(z_t-z')}}{[\kappa_F^2+(\mathbf{G}+\mathbf{K})^2]^{1/2}}e^{\pm i(\mathbf{G}+\mathbf{K})\cdot\mathbf{R}_t} \quad (z'+R_0<z_t)\ , \tag{8}$$

$$J_\pm(\mathbf{G}+\mathbf{K};z')\equiv\int_{-\infty}^{+\infty}dx'\int_{-\infty}^{+\infty}dy'\left[\frac{\partial}{\partial z'}\frac{e^{-\kappa_F|\mathbf{r}_t-\mathbf{r}'|}}{|\mathbf{r}_t-\mathbf{r}'|}\right]e^{\pm i(\mathbf{G}+\mathbf{K})\cdot\mathbf{R}'}$$
$$=\frac{\partial I_\pm(\mathbf{G}+\mathbf{K};z')}{\partial z'}$$
$$=2\pi e^{-[\kappa_F^2+(\mathbf{G}+\mathbf{K})^2]^{1/2}(z_t-z')}e^{\pm i(\mathbf{G}+\mathbf{K})\cdot\mathbf{R}_t} \quad (z'+R_0<z_t)\ . \tag{9}$$

Substituting (2) and (3) into (1) using (8) and (9) finally leads to the desired expression for the tunneling current density within the Tersoff and Hamann theory:

$$\mathbf{j}^{\mathrm{TH}}(\mathbf{r})=\frac{\pi^2e^2\hbar^3\Omega_t D^{(t)}(E_F)}{m^2\kappa_F^2}c^2(R_0)V\frac{e^{-\kappa_F|\mathbf{r}_t-\mathbf{r}|}}{|\mathbf{r}_t-\mathbf{r}|}$$
$$\times\left[(\mathbf{r}_t-\mathbf{r})\frac{\kappa_F|\mathbf{r}_t-\mathbf{r}|+1}{|\mathbf{r}_t-\mathbf{r}|^2}-\nabla\right]$$
$$\times\int d\nu\,\delta(E_\nu-E_F)\psi_\nu^{(s)}(\mathbf{r}_t)^*\psi_\nu^{(s)}(\mathbf{r})\ , \tag{10}$$

where $D^{(t)}(E_F)$ is the Fermi-surface electronic density of states of the isolated tip electrode. The basic quantity describing the isolated sample electrode is the nonlocal spectral density $\int d\nu\,\delta(E_\nu-E_F)\psi_\nu^{(s)}(\mathbf{r}_t)^*\psi_\nu^{(s)}(\mathbf{r})$.

The total current is calculated by integrating the z component of Eq. (10) over any plane $z=$const lying in the vacuum region $0<z<z_t-R_0$. Using Eqs. (6) and (7) for the sample wave function and (8) and (9) for the surface integrals $I_\pm(\mathbf{G}+\mathbf{K};z)$ and $J_\pm(\mathbf{G}+\mathbf{K};z)$, the Tersoff-Hamann expression for the current is readily obtained:

$$I^{\mathrm{TH}}=\int_{-\infty}^{+\infty}dx\int_{-\infty}^{+\infty}dy\,j_z^{\mathrm{TH}}(\mathbf{r})$$
$$=\frac{8\pi^3\hbar^3c_t^2D_t(E_F)R_0^2e^{2\kappa_FR_0}}{m^2}e^2VN^{(s)}(\mathbf{r}_t;E_F)\ ,$$

where $N^{(s)}(\mathbf{r}_t;E_F)$ is the local electronic density of states of the sample at the Fermi energy.

Equation (10) is applied to two idealized samples in the next two sections.

III. JELLIUM SAMPLE

It is useful, as a basis of comparison, to know $\mathbf{j}^{\mathrm{TH}}(\mathbf{r})$ for the simplest model of the sample electrode, namely a half-space ($z<0$) of jellium. The electron wave function in the vacuum region outside the isolated jellium electrode is given by (6) with $\{\mathbf{G}\}=\mathbf{G}_0=0$ because of the lateral homogeneity:

$$\psi_{E,\mathbf{K}}^{(s)}(\mathbf{r})=\frac{-2^{1/2}ik_ze^{-\alpha_{\mathbf{K}}(0)z}e^{i\mathbf{K}\cdot\mathbf{R}}}{\Omega_s^{1/2}[\alpha_{\mathbf{K}}(0)-ik_z]} \quad (z>0)\ , \tag{11}$$

where $E\equiv\hbar^2(K^2+k_z^2)/2m$ and $\alpha_{\mathbf{K}}(0)\equiv(\kappa^2+K^2)^{1/2}$ with $\kappa^2=2m(V_0-E)/\hbar^2$. The coefficient $a_{E,\mathbf{K}}(0)$ was obtained by matching (6) onto the interior ($z<0$) wave function

$$\psi_{E,\mathbf{K}}(\mathbf{r})=[A\exp(ik_zz)+B\exp(-ik_zz)]\exp(i\mathbf{K}\cdot\mathbf{R})$$

in the usual way and normalizing the wave function to unity over a volume $\Omega_s=L^3$ of sufficiently large size [$L\gg k_z^{-1},\alpha_{\mathbf{K}}(0)^{-1}$]. [The wave function (11) is much simpler than the corresponding one in Lang's papers because it does not include the effect of self-consistent redistribution of charge via simultaneous solutions of the Schrödinger and Poisson equations.] The required nonlocal spectral density is

$$\int d\nu\,\delta(E_\nu-E_F)\psi_\nu^{(s)}(\mathbf{r}_t)^*\psi_\nu^{(s)}(\mathbf{r})$$
$$=\frac{\Omega_s}{(2\pi)^3}\int_0^\infty dk_z\int_0^\infty dK\int_0^{2\pi}K\,d\theta\,\delta\left[\frac{\hbar^2}{2m}(K^2+k_z^2)-E_F\right]\frac{2}{\Omega_s}\frac{k_z^2e^{-(\kappa^2+K^2)^{1/2}(z_t+z)}e^{i\mathbf{K}\cdot(\mathbf{R}-\mathbf{R}_t)}}{\kappa^2+K^2+k_z^2}$$
$$=\frac{1}{V_0(2\pi)^2}\int_0^{(2mE_F)^{1/2}/\hbar}dk_zk_z^2J_0((2mE_F/\hbar^2-k_z^2)^{1/2}|\mathbf{R}-\mathbf{R}_t|)e^{-(2mV_0/\hbar^2-k_z^2)^{1/2}(z_t+z)}\ . \tag{12}$$

Evaluation of the partial derivative of the spectral density with respect to z is trivial, as are those with respect to x and y [using $dJ_0(u)/du = -J_1(u)$].

Figures 1(a) and 1(b) are vector plots for the projection of the tunneling current density $\mathbf{j}^{\mathrm{TH}}(\mathbf{r})$ onto the planes $x = x_t$ and $z = z_t/2$, respectively, with the length of each arrow scaled by $[\,|\,\mathbf{j}^{\mathrm{TH}}(\mathbf{r})\,|\,/\,|\,\mathbf{j}^{\mathrm{TH}}(\mathbf{r})\,|_{\max}]^p$ with $p = 0.3$. Figures 1(c) and 1(d) are contour plots of $j_z^{\mathrm{TH}}(x_t,y,z)$ and $j_z^{\mathrm{TH}}(x,y,z_t/2)$, respectively. The position of the tip, $\mathbf{r}_t$, is indicated by a solid circle. All the plots are for the same values of k_F (1.7 Å^{-1}) and work function $\overline{\Phi} \equiv V_0 - E_F$ (4.2 eV) as used in the next section for a monolayer of graphite and for $z_t = 20a_0$ (a_0 is the Bohr radius). Results are shown only for $2a_0 \leq z \leq 18a_0$ reflecting (in a token way) the fact that the transfer Hamiltonian approximation is not valid near the edges of the tunneling barrier and also that z must be less than $z_t - R_0$. The z cutoffs used here are probably too liberal so that qualitative behavior is understood in the suspect regions near the top and bottom edges of Figs. 1(a) and 1(c) [and also Figs. 3(a), 3(c), 4(a), and 4(c) of Sec. IV].

The results in Fig. 1 are in good qualitative agreement with those of Lang when one allows for the fact that $j_z^{\mathrm{TH}}(\mathbf{r})$ approaches zero for large values of $|\,\mathbf{R}_t - \mathbf{R}\,|$ rather than leveling off at a nonzero value, reflecting the very different lateral structure of the respective model tips. The current distribution of Fig. 1 will be contrasted with the corresponding ones for a monolayer of graphite in the next section.

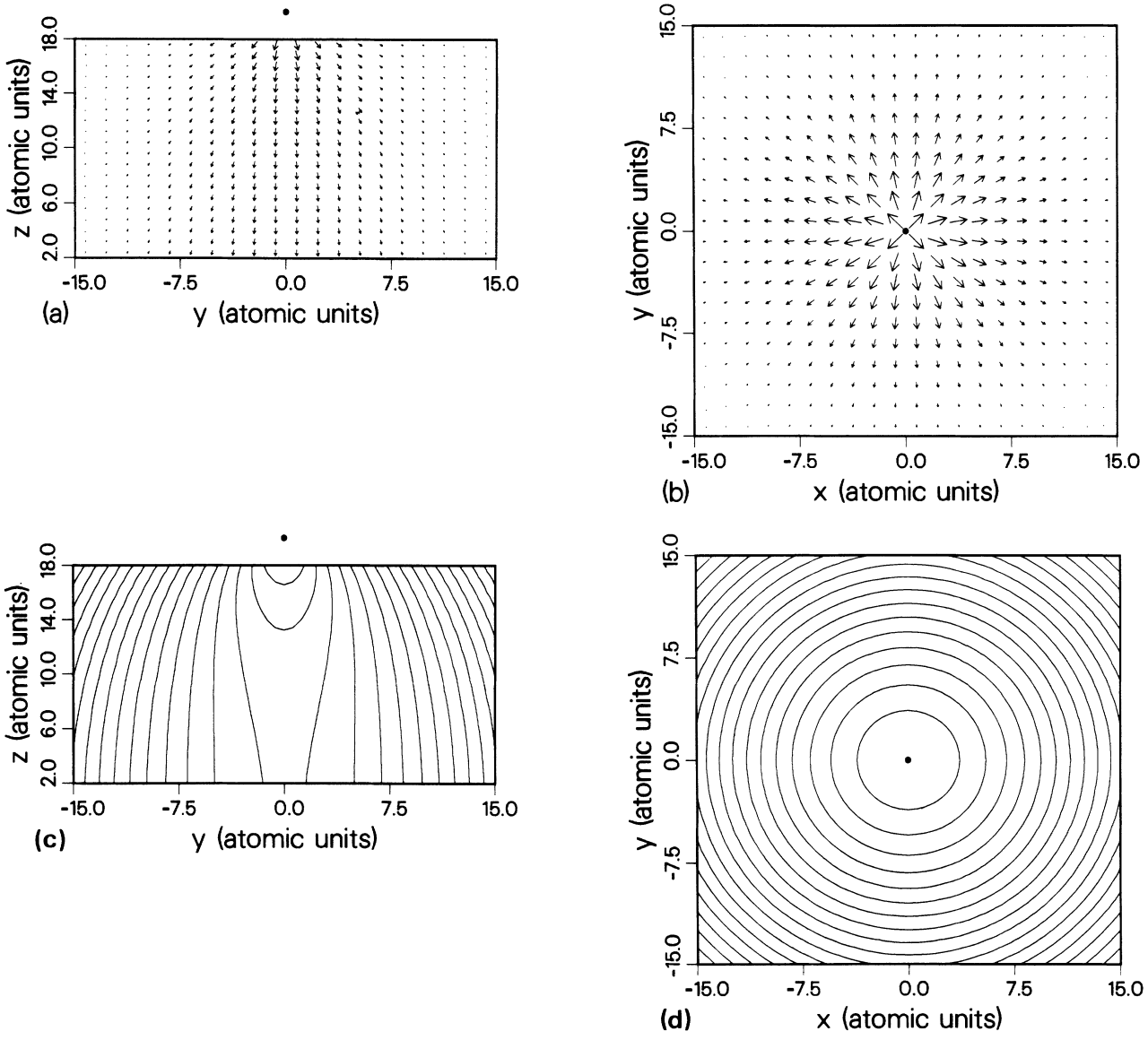

FIG. 1. Distribution of the tunneling current for a jellium sample. Vector plots for the projection of $\mathbf{j}^{\mathrm{TH}}(\mathbf{r})$ onto the planes (a) $x = x_t$ and (b) $z = z_t/2$, with the length of each arrow scaled by $[\,|\,\mathbf{j}^{\mathrm{TH}}(\mathbf{r})\,|\,/\,|\,\mathbf{j}^{\mathrm{TH}}(\mathbf{r})\,|_{\max}]^p$ with $p = 0.3$. Contour plots of the z component of the tunneling current density, $j_z^{\mathrm{TH}}(\mathbf{r})$, for the planes (c) $x = x_t$ and (d) $z = z_t/2$, with each successive contour, proceeding away from the tip, depicting a factor-of-2 decrease in $|\,j_z^{\mathrm{TH}}\,|$. The position of the model tip is indicated by a solid circle.

IV. MONOLAYER OF GRAPHITE

STM images of graphite[10–14] are remarkable in several respects: the lateral resolution is such that individual carbon atoms only 1.4 Å apart are clearly resolved; the STM constant-current corrugations measured under clean conditions are much larger ($\sim$0.9 Å) than the corrugations in the total charge density ($\sim$0.2 Å) expected from helium-atom scattering experiments[15] and electronic-structure calculations;[16] very much larger corrugations (up to tens of angstroms) have been observed[13,14] under nonideal conditions and attributed to tip-induced deformation of the graphite surface[13,14,17,18] mediated by a contamination layer.[13,17]

Recently, Tersoff[9] investigated the problem of the anomalously large corrugations observed under clean conditions. He neglected the very weak interlayer coupling and calculated the STM constant-current image for a monolayer of graphite. Within a six-plane-wave approximation, it is a zero-band-gap semiconductor with a Fermi surface consisting of only two distinct points at opposite corners of the hexagonal surface Brillouin zone [see Fig. 2(b)]. Far enough into the vacuum region ($z>0$), a three-plane-wave model for each of the two Fermi-surface wave functions is adequate and the local density of electronic states at the Fermi energy is given by[9]

$$N^{(s)}(\mathbf{r};E_F)\propto\left[\sin^2\left[\frac{\sqrt{3}}{2}K_F y\right]+\sin^2\left[\frac{\sqrt{3}}{4}K_F(\sqrt{3}x-y)\right]+\sin^2\left[\frac{\sqrt{3}}{4}K_F(\sqrt{3}x+y)\right]\right]e^{-2\alpha_F z}, \quad (13)$$

where $K_F=4\pi/3a$, with a the lattice constant, is the length of the two-dimensional Fermi wave vector and $\alpha_F\equiv(2m\Phi/\hbar^2+K_F^2)^{1/2}$ with Φ the graphite work function. (13) has a hexagonal array of nodal lines, $\{x=ma/2,\ y=n\sqrt{3}a/2:\ m,n=\ldots,-2,-1,0,1,2,\ldots;\ m-n$ even$\}$, passing through the centers of the carbon hexagons [see Fig. 2(a)]. Since $I^{\mathrm{TH}}\propto N^{(s)}(\mathbf{r}_t;E_F)$, the tunneling current is zero when the center of the model tip lies along one of these lines and hence the constant-current image has a corresponding hexagonal array of singular dips. In actual graphite these singularities will be smoothed out by various effects[9] such as corrections to the model-tip wave function, nonideal instrumental response, and tunneling to states with $\mathbf{K}$ not exactly equal to $\mathbf{K}_F$ because of finite bias and/or finite Fermi surface arising from the effect of additional plane waves and weak coupling between the layers. It has recently been shown[19] that the relative motion of the tip and graphite atoms due to thermal lattice vibrations can readily provide enough smoothing to account for the finite but anomalously large corrugation of $\sim$0.9 Å observed at room temperature.

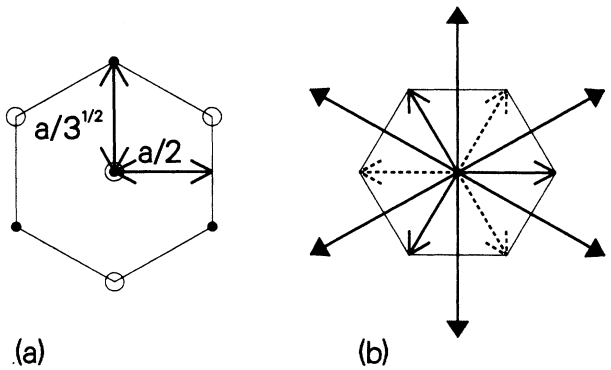

FIG. 2. Real-space and reciprocal-space unit cells for a monolayer of graphite. (a) Hexagonal unit cell in real space. The lattice constant a is 2.46 Å. There is a carbon atom at each corner of the hexagon. Each of the two distinct Fermi surface wave functions has a nodal line passing through the center of the hexagon and through three of the six corners. The nodes of one are indicated by ○ and of the other by ●. (b) Hexagonal first Brillouin zone. The two distinct sets of three equivalent (modulo a reciprocal-lattice vector $\mathbf{G}$) Fermi wave vectors, $\mathbf{K}_F$, are indicated by solid and dashed arrows terminating at corners. The six shortest nonzero reciprocal-lattice vectors are shown by the long arrows.

For Tersoff's six-plane-wave description of a monolayer of graphite it is easy to construct the nonlocal spectral density entering Eq. (10) for $\mathbf{j}^{\mathrm{TH}}(\mathbf{r})$. The two distinct Fermi-surface wave functions are

$$\psi^{(1)}_{\mathbf{K}_F}(\mathbf{r})=N(e^{iK_F x}+e^{i2\pi/3}e^{-i(K_F/2)(x-\sqrt{3}y)}+e^{i4\pi/3}e^{-i(K_F/2)(x+\sqrt{3}y)})e^{-\alpha_F z}, \quad (14)$$

$$\psi^{(2}_{\mathbf{K}_F})(\mathbf{r})=N(e^{-iK_F x}+e^{i2\pi/3}e^{i(K_F/2)(x-\sqrt{3}y)}+e^{i4\pi/3}e^{i(K_F/2)(x+\sqrt{3}y)})e^{-\alpha_F z}. \quad (15)$$

These wave functions were each constructed from the three plane waves, $\exp(i\mathbf{K}_F\cdot\mathbf{R})$, having equivalent (modulo a reciprocal-lattice vector $\mathbf{G}$) Fermi wave vectors, for example, $\mathbf{K}_F=K_F\hat{\mathbf{x}}$, $K_F(-\hat{\mathbf{x}}+\sqrt{3}\hat{\mathbf{y}})/2$, and $-K_F(\hat{\mathbf{x}}+\sqrt{3}\hat{\mathbf{y}})/2$ for (14) [see Fig. 2(b)]. Each of the wave functions (14) and (15) has nodal lines running through the center and through every other corner of each carbon hexagon, with the corner nodes of (14) alternating with those of (15) so that only the nodal lines through the centers are common to both, [see Fig. 2(a)]. It is clear from Eq. (10) that when the tip lies directly above the center of a carbon hexagon the tunneling current density $\mathbf{j}^{\mathrm{TH}}(\mathbf{r})$ is zero everywhere. To make contact with actual graphite, smoothing is introduced[19] by allowing the tip atom to fluctuate about its equilibrium position with root-mean-square displacements in the x, y, and z directions of 0.1 Å (a rectangular fluctuation distribution function is assumed for each direction). The effect of this smoothing is to reduce the singular corrugation in the constant-current image[9] to 0.9 Å (Ref. 19) while producing a more realistic current-density map for the situation in which the tip lies directly above the center of a carbon ring. The smoothing has no appreciable effect when the tip is directly above a carbon atom. (In actual graphite, neighboring carbon atoms in the hexagonal ring are inequivalent because one is directly above an atom in the second layer while the other is not.)

Before presenting numerical current distributions for a monolayer of graphite it is instructive to look at the functional form of $j_z^{\mathrm{TH}}(\mathbf{r})\equiv\mathbf{j}^{\mathrm{TH}}(\mathbf{r})\cdot\hat{\mathbf{z}}$. Substituting the wave

functions (14) and (15) into (10) immediately leads to

$$j_z^{\mathrm{TH}}(\mathbf{r}) \propto \frac{e^{-\kappa_F |\mathbf{r}_t-\mathbf{r}| - \alpha_F(z+z_t)}}{|\mathbf{r}_t-\mathbf{r}|} \times \left[(z_t-z)\frac{\kappa_F |\mathbf{r}_t-\mathbf{r}|+1}{|\mathbf{r}_t-\mathbf{r}|^2}+\alpha_F\right] f(x_t,y_t;x,y) .$$

It readily follows, using $K_F = 1.7$ Å^{-1} and $\alpha_F = 2.0$ Å^{-1}, that

$$[f(x_t,y_t;x,y)]^{-1}\left[\frac{\partial j_z^{\mathrm{TH}}(\mathbf{r})}{\partial z}\right]_{\mathbf{r}_t,\mathbf{R}} < 0 \quad (z_t - z \gtrsim 1.2 \text{ Å}) . \quad (16)$$

The restriction $z_t - z \gtrsim 1.2$ Å is really no restriction at all because $z_t - z$ is already required to be larger than R_0 and it is hard to conceive of R_0 being any smaller than the radius of the single atom believed to lie at the very end of a high-resolution STM tip. Moreover the transfer Hamiltonian approach is suspect for such a small value of $z_t - z$. Hence, over the practical range of z the magnitude of $j_z^{\mathrm{TH}}(\mathbf{r})$ at fixed $\mathbf{r}_t$ and $\mathbf{R} \equiv (x,y)$ decreases with increasing z, i.e., increases towards the graphite sample. Since the current flow must spread out laterally in going from a sharp tip to an extended sample, conservation of current requires that $j_z^{\mathrm{TH}}(\mathbf{r})$ must take on both positive and negative values over any plane $z = \text{const}$ $(0 \le z \le z_t - R_0)$. This surprising prediction is borne out by the numerical calculations.

Figures 3(a) and 3(b) are vector plots for the projec-

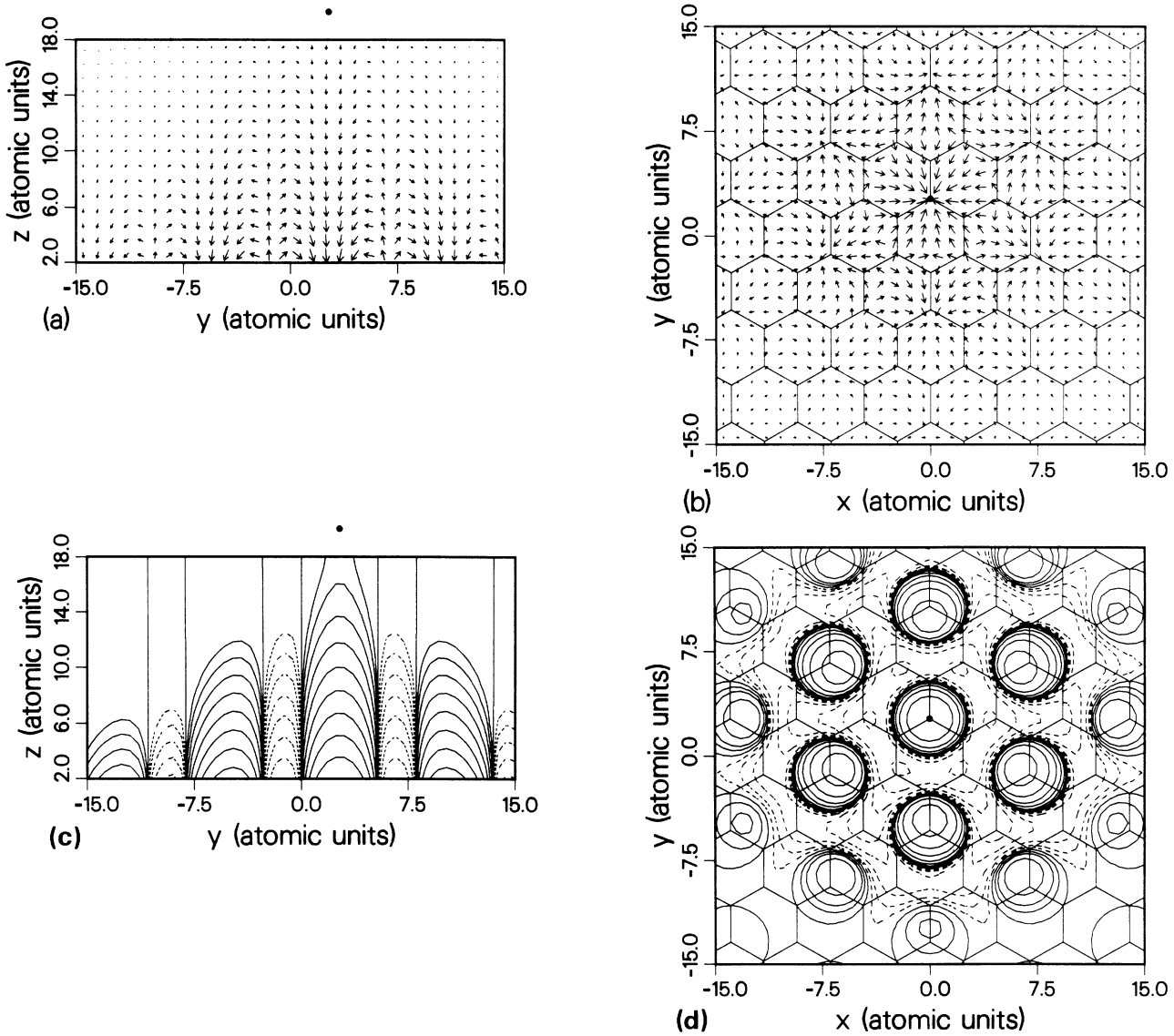

FIG. 3. Distribution of the tunneling current for a graphite monolayer sample when the tip (●) is positioned directly above a carbon atom. Vector plots for the projection of $\mathbf{j}^{\mathrm{TH}}(\mathbf{r})$ onto the planes (a) $x = x_t$ and (b) $z = z_t/2$, with the length of each arrow scaled by $[\,|\mathbf{j}^{\mathrm{TH}}(\mathbf{r})|\,/\,|\mathbf{j}^{\mathrm{TH}}(\mathbf{r})_{\max}|\,]^p$ with $p = 0.2$. Contour plots of the z component of the tunneling current density, $j_z^{\mathrm{TH}}(\mathbf{r})$, for the planes (c) $x = x_t$ and (d) $z = z_t/2$, with contours of negative j_z^{TH} indicated by solid lines and positive by dashed lines. Adjacent contours correspond to a factor-of-2 change in $|j_z^{\mathrm{TH}}|$ with the positive and negative contours treated separately. In (c) $|j_z^{\mathrm{TH}}|$ increases towards the sample along any line perpendicular to the sample. In (d) the amplitude of the oscillations in j_z^{TH} increases towards the projected tip position.

tions of $\mathbf{j}^{TH}(\mathbf{r})$ onto the planes $x=x_t$ and $z=z_t/2$, respectively, scaled by $[\,|\mathbf{j}^{TH}(\mathbf{r})|/|\mathbf{j}^{TH}(\mathbf{r})|_{max}]^p$ with $p=0.2$; Figs. 3(c) and 3(d) are contour plots of $j_z^{TH}(x_t,y,z)$ and $j_z^{TH}(x,y,z_t/2)$, respectively, all for $z_t=20a_0$ with the (stationary) model tip directly above a carbon atom. Figures 4(a) to 4(d) pertain to the case where the (vibrating) tip is directly above the center of a carbon hexagon [with a stationary tip $\mathbf{j}^{TH}(\mathbf{r})=0$ for all $\mathbf{r}$]. It is instructive to compare these plots with the corresponding ones for jellium.

Figure 1(a) is a scaled ($p=0.3$) vector plot of the projection of $\mathbf{j}^{TH}(\mathbf{r})$ onto the plane $x=x_t$ for the special case of a thick jellium slab as the sample electrode. The arrows fan out from the tip (indicated by ●) with $j_z^{TH}(\mathbf{r})$ always negative and with $|j_z^{TH}(x_t,y,z)|$ decreasing towards the sample along lines of constant y in the important region of small $|y-y_t|$. The corresponding scaled ($p=0.2$) vector plots for a monolayer of graphite with the tip directly above a carbon atom, Fig. 3(a), or directly above the center of a carbon ring, Fig. 4(a), are qualitatively different: $j_z^{TH}(x_t,y,z)$ oscillates in sign along any line $z=$const $(0<z<z_t-R_0)$ and $|j_z^{TH}(x_t,y,z)|$ increases towards the sample along any line $y=$const. These differences are shown more graphically in Figs. 1(c), 3(c), and 4(c) for the corresponding contours of constant $j_z^{TH}(x_t,y,z)$, with solid lines indicating negative ($j_z^{TH}<0$) contours and the dashed lines positive ($j_z^{TH}>0$) contours. Figures 1(b), 3(b), and 4(b) are scaled vector plots of the projection of $\mathbf{j}^{TH}(\mathbf{r})$ onto the plane $z=z_t/2$. For the monolayer of graphite, Figs. 3(b) and 4(b), the arrows are superimposed on a hexagonal lattice to indicate the positions of the carbon atoms. For jellium, Fig. 1(b),

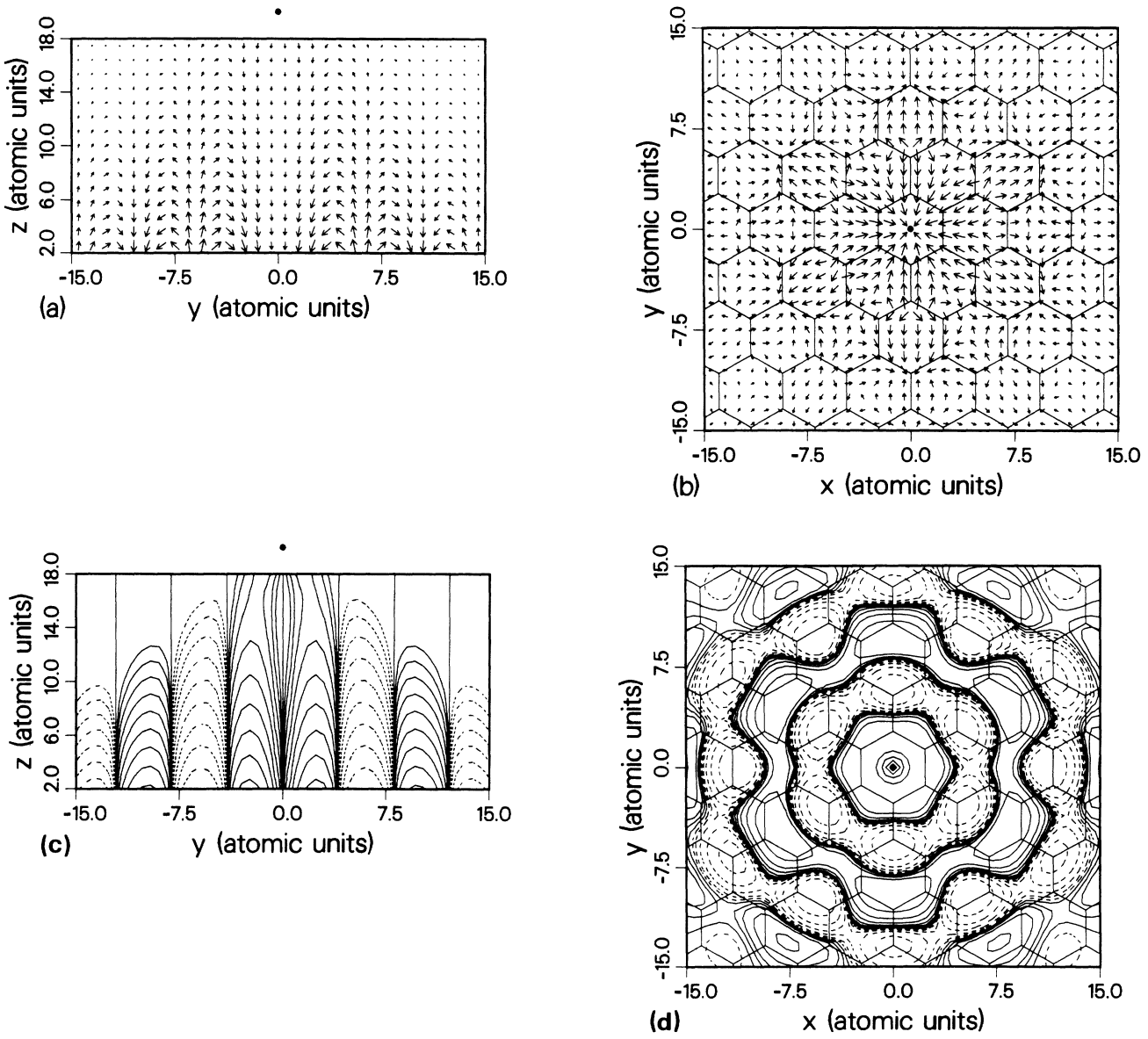

FIG. 4. Distribution of the tunneling current for a graphite monolayer sample when the (vibrating) tip is positioned (on average) directly above the center of a ring of six carbon atoms. The tip is vibrated in all three dimensions with root-mean-square displacement $\langle\delta_{x,y,z}^2\rangle^{1/2}=0.1$ Å. For a stationary tip directly above the center $\mathbf{j}^{TH}(\mathbf{r})=0$ for all $\mathbf{r}$. See the caption of Fig. 3 for details.

the flow of current is, of course, radially outward from the (projected) tip position (●). For graphite, Figs. 3(b) and 4(b), the flow is inward (for z not too near z_t) in the immediate vicinity of $(x=x_t, y=y_t)$. Further out the flow pattern becomes quite complex as current is funneled laterally through the vertical boundaries separating regions of negative j_z^{TH} from the adjacent positive regions. Such boundaries are obvious in Figs. 3(d) and 4(d) which show contours of constant $j_z^{\mathrm{TH}}(x,y,z_t/2)$, with solid lines indicating negative contours and dashed lines positive contours. For the case in which the tip is directly above a carbon atom the negative regions consist of disjoint vertical tubes embedded in a single interconnected positive region. When the (vibrating) tip is directly above the center of a carbon ring the central negative region is surrounded by corrugated cylindrical rings of alternating positive and negative j_z^{TH}. The contours of Figs. 3(d) and 4(d) are in marked contrast to the monotonic circularly symmetric contours of $j_z^{\mathrm{TH}}(x,y,z_t/2)$ for jellium shown in 1(d).

The calculated current distributions were checked for both jellium and graphite (for both tip positions) by computing the total current by integration of $j_z^{\mathrm{TH}}(\mathbf{r})$ over various z planes between tip and sample. The computed values were independent of the plane chosen to high accuracy. In addition, $[\nabla\cdot\mathbf{j}^{\mathrm{TH}}(\mathbf{r})]/|\mathbf{j}^{\mathrm{TH}}(\mathbf{r})/a|$ was computed at a large number of points for each system to confirm that $\nabla\cdot\mathbf{j}^{\mathrm{TH}}(\mathbf{r})=0$ was well satisfied.

Also of interest is the convergence as the z component of the current density is integrated outwards from the (projected) tip position on a plane of constant z to obtain the current. Figure 5 shows the 50% and 90% radii, $\rho_{0.5}$ and $\rho_{0.9}$, as functions of z_t-z for jellium and a graphite monolayer when the tip is directly above a carbon atom. The rate of increase of both $\rho_{0.5}$ and $\rho_{0.9}$ is much greater for graphite than for jellium. For $z=z_t/2=10a_0$, $\rho_{0.5}$ and $\rho_{0.9}$ for graphite are greater than the corresponding quantities for jellium by factors of $2\frac{1}{2}$ and 2, respectively. The relatively slow lateral decay of j_z^{TH} for a monolayer of graphite is at first sight surprising in view of the remarkable lateral resolution apparent in experimental STM images of actual graphite. There is no paradox, however, because a very narrow current filament is a sufficient but not necessary condition for high lateral resolution. The lateral resolution is determined by the sensitivity of the *total* tunneling current to the lateral position (x_t,y_t) of the tip at constant z_t. Because of its peculiar electronic structure, with only two distinct states at the Fermi surface, a graphite monolayer is an example of a system in which the total tunneling current changes significantly with lateral tip position on a much shorter length scale than that characteristic of the lateral decay of the tunneling current density for fixed tip position.

V. CONCLUDING DISCUSSION

In this paper a simple expression for the tunneling current density within the STM theory of Tersoff and Hamann[1] was derived from the more general expression due to Lang.[2–4] It was used to investigate the current distribution in the vacuum region between a monolayer of graphite and the model STM tip. The current distribution is qualitatively different than that for jellium: for fixed $\mathbf{r}_t$ and $\mathbf{R}\equiv(x,y)$, $|j_z^{\mathrm{TH}}(\mathbf{r})|$ increases monotonically towards the sample; $j_z^{\mathrm{TH}}(\mathbf{r})$ takes on both positive and negative values in a complicated flow pattern; and the lateral falloff of the current density away from the (projected) tip position is much slower than one might intuitively expect from the remarkable lateral resolution (~1 Å) obtained for graphite using the STM. The results for a monolayer of graphite show that a sharp peak in the tunneling current density directly under the tip is not a necessary condition for high lateral resolution with the STM. Ironically, it is graphite, which exhibits the best lateral resolution of any system studied to date, that provides the best example to illustrate this point.

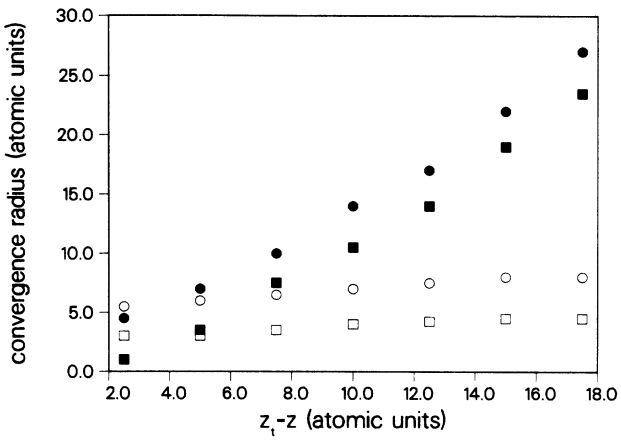

FIG. 5. Dependence on z_t-z of the convergence of the tunneling current as $j_z^{\mathrm{TH}}(x,y,z)$ is integrated outwards from the projected tip position on a plane of constant z. The 50% and 90% radii, $\rho_{0.5}$ and $\rho_{0.9}$, for a jellium sample are indicated by □ and ○, respectively. The same quantities for a monolayer of graphite with the tip located directly above a carbon atom are indicated by ■ and ●, respectively.

Although the position-momentum uncertainty relations forbid direct measurement of the STM tunneling current density it is an important quantity in the understanding of certain phenomena such as local heating of the sample surface and selective excitation of individual adatoms by the tunneling current. Since such phenomena involve the tunneling current density in the immediate vicinity of the sample surface there is a definite need to go beyond the transfer-Hamiltonian approach which breaks down in this region. When a better theory is available it will be interesting to see to what extent the remarkable properties presented here for a monolayer of graphite are modified.

Note added in proof. Stoll *et al.*[20] investigated the current distribution between two periodically corrugated free-electron-metal electrodes separated by a constant potential barrier. The two-dimensional periodicity for the array of tips was a large integral multiple of that for the sample surface so that the current density associated with a supercell approximated the current density in the vicinity of a single isolated tip on an otherwise planar probe electrode. For a single $\mathbf{K}_F$ component of the current density they found that current loops close to the sample

surface were possible due to strong interference between the incoming and reflected electron waves. Since the Fermi surfaces of both metals were of typical finite extent these loops disappeared when the contributions of all $\mathbf{K}_F$ were summed.

ACKNOWLEDGMENTS

It is a pleasure to thank R. Blake and J. E. Inglesfield (S.E.R.C., Daresbury, England) for useful discussions.

[1]J. Tersoff and D. R. Hamann, Phys. Rev. Lett. **50**, 1998 (1983); Phys. Rev. B **31**, 805 (1985).
[2]N. D. Lang, Phys. Rev. Lett. **55**, 230 (1985).
[3]N. D. Lang, Phys. Rev. Lett. **56**, 1164 (1986).
[4]N. D. Lang, IBM J. Res. Dev. **30**, 374 (1986).
[5]N. D. Lang, Phys. Rev. B **34**, 5947 (1986).
[6]N. D. Lang, Phys. Rev. Lett. **58**, 45 (1987).
[7]J. Bardeen, Phys. Rev. Lett. **6**, 57 (1961).
[8]They did make the usual approximations of ignoring the image potential and using an average work function in place of the individual work functions for the two electrodes.
[9]J. Tersoff, Phys. Rev. Lett. **57**, 440 (1986).
[10]G. Binnig, H. Fuchs, Ch. Gerber, H. Rohrer, D. Stoll, and E. Tosatti, Europhys. Lett. **1**, 31 (1986).
[11]S. Park and C. F. Quate, Appl. Phys. Lett. **48**, 112 (1986).
[12]P. K. Hansma, Bull. Am. Phys. Soc. **30**, 251 (1985).
[13]H. J. Mamin, E. Ganz, D. W. Abraham, R. E. Thomson, and J. Clarke, Phys. Rev. B **34**, 9015 (1986).
[14]J. M. Soler, A. M. Baro, N. García, and H. Rohrer, Phys. Rev. Lett. **57**, 444 (1986).
[15]G. Boata, P. Cantini, and R. Tatarek, Phys. Rev. Lett. **40**, 887 (1978); W. E. Carlos and M. W. Cole, Surf. Sci. **91**, 339 (1980).
[16]A. Selloni, P. Carnevali, E. Tosatti, and C. D. Chen, Phys. Rev. B **31**, 2602 (1985); I. P. Batra, N. García, H. Rohrer, H. Salemink, E. Stoll, and S. Ciraci, Surf. Sci. **181**, 126 (1987).
[17]J. H. Coombs and J. B. Pethica, IBM J. Res. Dev. **30**, 455 (1986).
[18]S. Ciraci and I. P. Batra, Phys. Rev. B **36**, 6194 (1987).
[19]C. R. Leavens, Phys. Rev. B **38**, 2169 (1988).
[20]E. Stoll, A. Baratoff, A. Selloni, and P. Carnevali, J. Phys. C **17**, 3073 (1984).